catalysts

MDPI

Article

Enhanced Catalytic Ozonation of Formaldehyde over MOFs-Derived MnO_x Catalysts with Diverse Morphologies: The Role of Oxygen Vacancies

Yulin Sun [1], Yiwei Zhang [1], Yong He [1,2], Wubin Weng [1,2], Yanqun Zhu [1,2,*] and Zhihua Wang [1,2]

[1] State Key Laboratory of Clean Energy Utilization, Zhejiang University, Hangzhou 310027, China; sunyulin@zju.edu.cn (Y.S.); yiwei_zhang@zju.edu.cn (Y.Z.); heyong@zju.edu.cn (Y.H.); wengwubin@zju.edu.cn (W.W.); wangzh@zju.edu.cn (Z.W.)
[2] Qingshanhu Energy Research Center, Zhejiang University, Hangzhou 311300, China
* Correspondence: yqzhu@zju.edu.cn; Tel.: +86-571-8795-2281

Abstract

Metal–organic frameworks (MOFs) have become a hot topic in various research fields nowadays. And MOF-derived metal oxides prepared by the sacrificial template method have been widely applied as catalysts for pollutant removal. Accordingly, we prepared a series of MOF-derived MnO_x catalysts with diverse morphologies (rod-like, flower-like, slab-like) via the pyrolysis of MOF precursors, and the as-prepared MnO_x catalysts demonstrated superior performance compared to the one prepared using the co-precipitation method. MnO_x-II, with a flower-like structure, exhibited excellent activity for formaldehyde (HCHO) catalytic ozonation at room temperature, reaching complete HCHO conversion at O_3/HCHO of 1.5 and more than 90% CO_2 selectivity at an O_3/HCHO ratio of 2.5. On the basis of various characterization methods, it was clarified that the enhanced catalytic performance of MnO_x-II benefited from its larger BET surface area, abundant oxygen vacancies, better redox ability at lower temperature, and more Lewis acid sites. The H_2O resistance and stability tests were also conducted. Furthermore, DFT calculations substantiated the enhanced adsorption of HCHO and O_3 on oxygen vacancies, while in–situ DRIFTS measurements elucidated the degradation pathway of HCHO during catalytic ozonation through detected intermediates.

Keywords: metal-organic-frameworks; manganese oxides; catalytic ozonation; formaldehyde; DFT calculations

Academic Editors: Edward G. Gillan and Jinxing Chen

Received: 17 June 2025
Revised: 31 July 2025
Accepted: 1 August 2025
Published: 6 August 2025

Citation: Sun, Y.; Zhang, Y.; He, Y.; Weng, W.; Zhu, Y.; Wang, Z. Enhanced Catalytic Ozonation of Formaldehyde over MOFs- Derived MnO_x Catalysts with Diverse Morphologies: The Role of Oxygen Vacancies. *Catalysts* **2025**, *15*, 752. https://doi.org/10.3390/catal15080752

1. Introduction

Driven by the accelerating urbanization and industrialization trends, the emission of gaseous pollutants has increased significantly, causing great damage to air quality worldwide. Typically, volatile organic compounds (VOCs), as crucial atmospheric pollutants, consistently induce adverse health effects and air quality issues, like dust haze and photochemical smog [1]. Common in indoor environments, formaldehyde (HCHO) usually leads to respiratory problems and lung damage, and worse yet, long exposure to HCHO even causes leukemia and cancers [2]. To mitigate the adverse effect of HCHO on the atmosphere and public health, developing efficient control means has become imperative.

Catalytic ozonation is a desirable method for pollution treatment, which can mineralize VOCs into harmless products (H_2O and CO_2) without secondary pollution. With the promotion of ozone (O_3), the reaction temperature is further lowered due to its strong

oxidizability and produced free radicals ($\cdot O^{2-}$, $\cdot O^{2-}$, $\cdot OH$) [3]. Moreover, the selection of catalysts with superior catalytic activity is important to impel the proceeding of the catalytic ozonation reaction. To date, numerous catalysts have been employed for HCHO degradation, involving precious metals (Au, Pt, Pd, etc.) [4–7] and non-precious metals (Mn, Co, etc.) [8,9]. However, the exorbitant price and deactivation tendency of precious metals restrict their practical application. Hence, efficient and economical catalysts are urgently required for HCHO removal.

Manganese oxides (MnO_x) have been widely applied to pollutant treatment as promising materials because of their low cost, multiple valence states, and diverse shapes [10]. Rational design strategies for better catalytic activity of MnO_x have been extensively investigated, such as regulating oxygen vacancies [11], adjusting morphologies [12], and altering preparation methods [13]. Zhao et al. [14] reported that the catalytic ozonation on MnO_x (O_3/HCHO=3:1) promoted the HCHO conversion (~100%) at ambient temperature, confirming the unique ability of ozone in promoting the performance of MnO_x under low temperature. Saputra et al. [15] systematically designed the morphologies of α-Mn_2O_3 (cubic, octahedral, truncated-octahedral), and the catalyst with a cubic shape exhibited higher catalytic activity for its bigger specific surface area and abundant active surface facets. Wang et al. [12] prepared several MnO_x catalysts with distinct morphologies (rod-, wire-, tubular-, and flower-like), and rod-like α-MnO_2 achieved complete toluene oxidation at lower temperatures, relating to its plentiful oxygen vacancies and reliable redox ability. Accordingly, the morphological control of MnO_x catalysts might prove to be critical to optimize catalytic performance.

Recently, MOFs have been intensively investigated in the catalysis field for some attractive advantages, including large surface area, controllable morphology, and high porosity [16–20]. With plenty of electron-deficient open metal sites, MOFs have strong interaction with VOCs and can easily adsorb and degrade pollution gases, which brings a broader prospect for VOC removal [21]. Furthermore, MOFs can be pyrolyzed as sacrificial precursors at high temperature in an aerobic atmosphere to fabricate diverse porous metal oxides, which can inherit the porosity and well-defined morphology of pristine MOFs [22]. By selecting appropriate precursors and control strategies, diverse morphologies of MOF-derived nano-structure catalysts can be rationally designed. Zhang et al. [23] researched the activity of Mn_2O_3 obtained from Mn-MOFs with different precursors (MIL-100, MOF-74, BTC). The catalyst derived from the cubic Mn-MIL-100 precursor performed well, associating with its higher Mn^{3+}/Mn^{4+} ratio and plentiful surface oxygen species. Li et al. [24] fabricated MOF-derived MnO_x-m catalysts with a nanorod-self-assembly hollow microsphere structure. Compared with other derivatives, the MnO_x-m catalysts presented superior catalytic performance due to their abundant exposed active sites, desirable redox ability, and plentiful active oxygen species. These studies illustrate that the catalyst performance is highly associated with morphological structures. However, there have been few studies on the catalytic ozonation of HCHO over MOF-derived MnO_x catalysts with different morphologies so far.

Herein, a series of MOFs-derived MnO_x catalysts with diverse structures were synthesized in this work via the pyrolysis of different MOFs precursors. The catalytic activity was evaluated through the measurement of HCHO conversion and CO_2 selectivity during the catalytic ozonation reaction at ambient temperature. Meanwhile, all kinds of characterization methods were adopted to illustrate the structure-activity relationship. Moreover, the intermediates generated during HCHO ozonation were also detected through in-situ DRIFTS analysis. Integrated with DFT calculation, the reaction mechanism was further clarified.

2. Results and Discussion

2.1. Catalytic Ozonation of HCHO

Figure 1a presents the catalytic performance of MnO_x catalysts during HCHO ozonation at room temperature by varying O_3/HCHO ratios (0.5~3.0). As shown in Equation (1), the complete mineralization of HCHO with ozone required a theoretical O_3/HCHO ratio of 2.0. Clearly, the increase in the O_3/HCHO ratio significantly improved the HCHO conversion of the catalysts. The O_3/HCHO ratio corresponding to 90% HCHO conversion (O_{90}) was the following sequence: MnO_x-II (1.1) < MnO_x-I (1.3) < MnO_x-III (1.4) < MnO_x-IV (1.8). Compared to the MOF-derived MnO_x catalysts, MnO_x-IV prepared by the co-precipitation method had undesirable catalytic activity, getting a 100% conversion at O_3/HCHO of 3.0. Meanwhile, MnO_x-II with a flower-like structure exhibited remarkably higher HCHO conversion, achieving 100% HCHO conversion when the O_3/HCHO ratio was 1.5. It was worth mentioning that almost no O_3 residual was observed during the catalytic tests.

$$HCHO + (2 - x)O_3 \rightarrow (1 - x)CO_2 + xCO + (2 - x)O_2 + H_2O \quad (1)$$

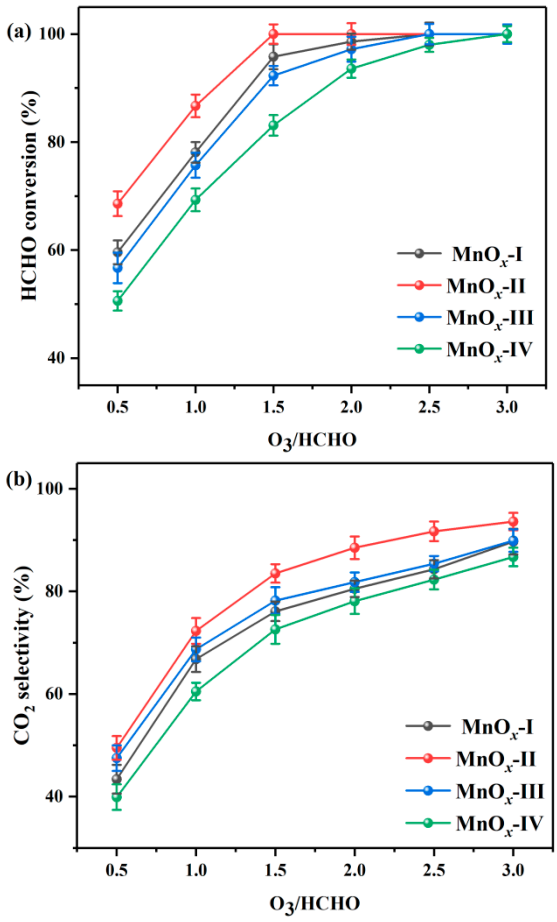

Figure 1. (**a**) HCHO conversion and (**b**) CO_2 selectivity during catalytic ozonation of HCHO over synthesized catalysts. (HCHO initial concentration: 30 ppm, T = 30 °C).

To reduce hazardous intermediates and promote green environmental protection, environmentally friendly CO_2 and H_2O are regarded as ideal final products. Consequently, the CO_2 selectivity results of MnO_x catalysts are shown in Figure 1b. Obviously, for all the catalysts, the CO_2 selectivity had a nearly linear increase with the O_3/HCHO ratio. And on the whole range of O_3 input, MnO_x-II maintained the highest CO_2 selectivity, which

attained above 90% CO_2 selectivity at an O_3/HCHO ratio of 2.5, and the order for the CO_2 selectivity was as follows: MnO_x-II > MnO_x-III > MnO_x-I > MnO_x-IV.

2.2. Catalyst Characterization

2.2.1. Crystalline Structures

The crystalline phases of the MnO_x catalysts were identified through XRD analysis (Figure 2). And the diffraction peaks at 23.1°, 32.9°, 38.2°, 45.1°, 49.3°, 55.1°, and 65.7° were ascribed to the (2 1 1), (2 2 2), (4 0 0), (3 3 2), (4 3 1), (4 4 0), and (6 2 2) planes of α-Mn_2O_3 (PDF#71-0636), while the weak peaks at 18.1°, 28.8°, and 36.6° were indexed to the (2 0 0), (3 1 0), and (4 0 0) plane of MnO_2 (PDF#44-0141) [25]. Compared with other MnO_x catalysts, MnO_x-I and MnO_x-II displayed a relatively weaker diffraction intensity, implying their smaller particle sizes, which introduced sufficient lattice defects and enhanced catalytic performance [26]. Moreover, the crystallite size was calculated by the Scherrer formula, and the crystallite sizes of MnO_x-I, MnO_x-II, MnO_x-III, and MnO_x-IV were 35.6 nm, 32.3 nm, 36.7 nm, and 37.2 nm, respectively. MnO_x-II showed the smallest crystallite size.

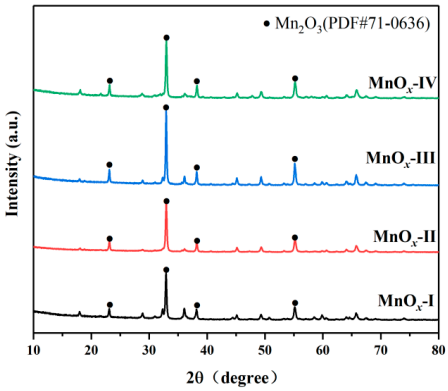

Figure 2. XRD patterns of prepared catalysts.

To explore the corresponding morphologies of MOF precursors and MOF-derived MnO_x catalysts, the images of SEM characterization are depicted in Figure 3. Clearly, MnO_x-I presented a rod-like structure composed of multiple stacked nanorods, while MnO_x-II exhibited a flower-like structure with ordered assembly nanosheets, and MnO_x-III consisted of many stacked slabs. Prepared by the co-precipitation method, MnO_x-IV showed an amorphous structure with agglomerated nanoparticles, which might result in a reduction in surface area. After calcination, the surface of MOF-derived MnO_x catalysts became rougher, and a lot of voids appeared, attributable to the thermolysis of organic ligands under thermal treatment. Fortunately, the morphologies of MOF precursors were basically retained on MOF-derived MnO_x catalysts, and the generated surface defects on porous structures accelerated both active site formation and VOCs–catalyst contact efficiency [27].

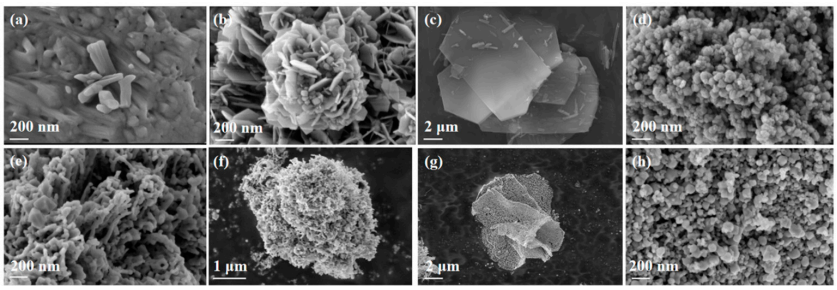

Figure 3. SEM images of (**a**) MnO_x-I, (**b**) MnO_x-II, (**c**) MnO_x-III, (**d**) MnO_x-IV before calcination; and (**e**) MnO_x-I, (**f**) MnO_x-II, (**g**) MnO_x-III, (**h**) MnO_x-IV after calcination.

2.2.2. Textual Properties

To explore the textual properties of MnO_x catalysts, their N_2 adsorption–desorption isotherms (Type IV, H3 hysteresis loop) and BJH pore size distributions are depicted (Figure S1). The BET surface area and pore volume are arranged in the sequence of MnO_x-II > MnO_x-I > MnO_x-III > MnO_x-IV (Table 1), in accord with the HCHO conversion sequence. Higher surface area usually promotes the generation of surface active sites, the adsorption of VOCs, and the activation of ozone [28,29]. With the optimal catalytic activity, MnO_x-II possessed a higher surface area and pore volume, 20.0 $m^2 \cdot g^{-1}$ and 0.079 $cm^3 \cdot g^{-1}$, respectively. Moreover, MnO_x-IV exhibited the least favorable catalytic activity in HCHO degradation, with lower surface area and pore volume.

Table 1. Textual properties of prepared catalysts.

Catalyst	BET Surface Area /$m^2 \cdot g^{-1}$	Pore Volume [a] /$cm^3 \cdot g^{-1}$	Average Pore Diameter [b]/nm
MnO_x-I	19.6	0.077	10.3
MnO_x-II	20.0	0.079	10.7
MnO_x-III	18.7	0.075	10.9
MnO_x-IV	15.8	0.044	16.0

[a] BJH desorption cumulative volume of pores. [b] BJH desorption average pore diameter.

2.2.3. Surface Properties

To research the valence states of elements on the catalyst surface, the XPS curves are depicted in Figure 4, and the content of elements after deconvolution is presented in Table 2. As displayed in Figure 4a, the binding energies at 641.4 and 643.3 eV were ascribed to Mn^{3+} and Mn^{4+} species, respectively [30,31]. The Mn^{3+}/Mn^{4+} ratio declined as the sequence MnO_x-II (1.85) > MnO_x-I (1.72) > MnO_x-III (1.48) > MnO_x-IV (1.44), fitting with the order of HCHO conversion. The existence of Mn^{3+} ions could promote the formation of oxygen vacancies through a charge balance mechanism [32]. Thus, a higher Mn^{3+}/Mn^{4+} ratio usually suggests more oxygen vacancies on the catalyst surface, which can promote the decomposition of ozone and the catalytic ozonation of VOCs [33].

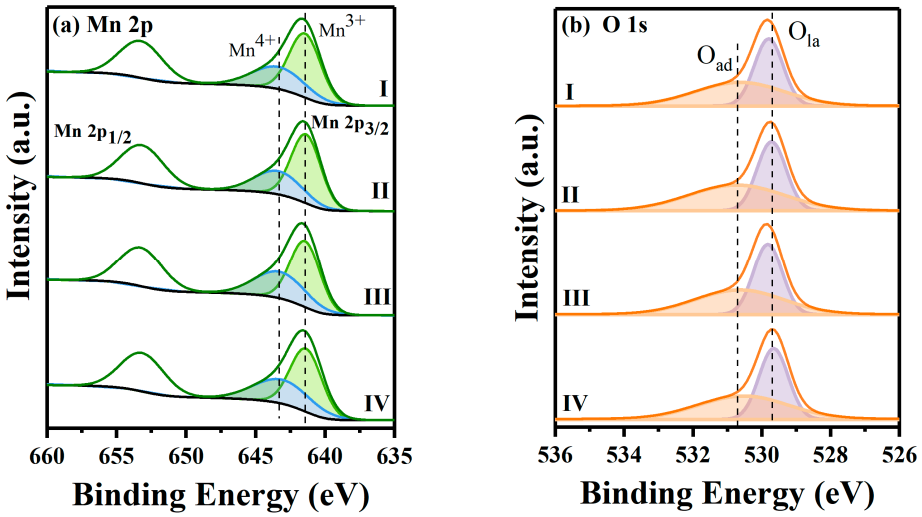

Figure 4. XPS spectra of (**a**) Mn 2p and (**b**) O 1 s for synthesized catalysts.

Table 2. XPS results of synthesized catalysts.

Catalysts	Mn 2 $p_{3/2}$		O 1 s		Mn^{3+}/Mn^{4+}	O_{ad}/O_{la}
	Mn^{4+} (%)	Mn^{3+} (%)	O_{la} (%)	O_{ad} (%)		
MnO_x-I	36.8	63.2	47.7	52.3	1.72	1.10
MnO_x-II	35.1	64.9	44.9	55.1	1.85	1.23
MnO_x-III	40.4	59.6	48.2	51.8	1.48	1.07
MnO_x-IV	40.9	59.1	49.3	50.7	1.44	1.03

The O 1s spectra identified lattice oxygen species (O_{la}) at 529.7 eV and adsorbed oxygen species (O_{ad}) at 530.7 eV, respectively (Figure 4b). Moreover, the ratio of O_{ad}/O_{la} ranked in order of MnO_x-II (1.23) > MnO_x-I (1.10) > MnO_x-III (1.07) > MnO_x-IV (1.03). Compared to O_{la} species, O_{ad} species showed higher oxygen mobility, which could accelerate oxygen vacancy generation and promote the reactant activation process [34,35].

To sum up, MnO_x-II had the highest Mn^{3+} and O_{ad} contents, which was conducive to increased oxygen vacancies and accelerated oxygen mobility. Different from the MOF-derived MnO_x catalysts, MnO_x-IV presented a lower Mn^{3+} and O_{ad} proportion, fitting with its undesirable catalytic efficiency. Moreover, the results of XPS analysis aligned with the HCHO conversion order, indicating the critical role of oxygen vacancies in affecting catalytic performance.

2.2.4. Temperature Programmed Studies

A Raman spectrum study was performed to explore the oxygen vacancies in MnO_x catalysts (Figure 5a). The characteristic peaks at 630~650 cm^{-1} corresponded to the v2(Mn−O) stretching vibration of [MnO_6] chains, while Mn−O bond strength usually correlates to oxygen vacancies formation [36]. Based on Hooke's law, the strength of the Mn−O bond was determined by the following equation (Equation (2)):

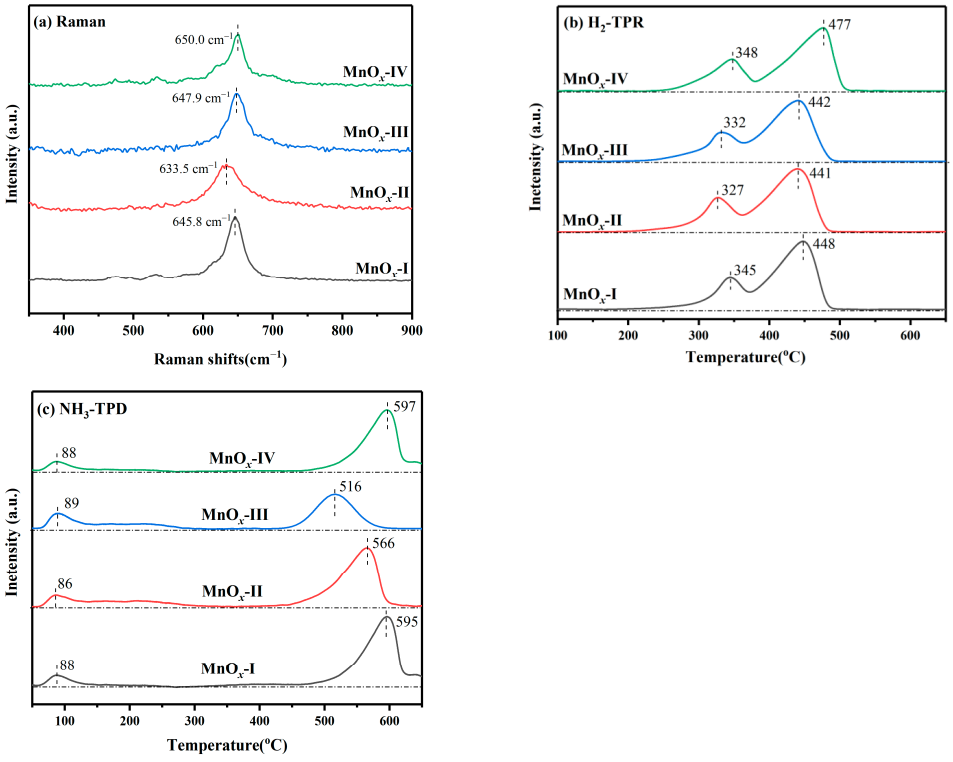

Figure 5. (**a**) Raman; (**b**) H_2-TPR; (**c**) NH_3-TPD profiles of synthesized catalysts.

$$\omega = \frac{1}{2\pi c}\sqrt{\frac{k}{\mu}} \quad (2)$$

where ω represents the stretching vibration shift, k refers to Mn−O bond strength, μ refers to effective mass and c represents the light velocity, respectively.

The ω value of catalysts decreased in the order: MnO_x-IV (650.0 cm^{-1}) > MnO_x-III (647.9 cm^{-1}) > MnO_x-I (645.8 cm^{-1}) > MnO_x-II (633.5 cm^{-1}). Performing well in catalytic activity, MnO_x-II showed the lowest ω value, which corresponded to the lowest strength. Weaker Mn−O bond strength indicates an increase in oxygen vacancy defects as well as higher oxygen mobility because of the easily stripped oxygen species, which can facilitate HCHO deep oxidation [37,38]. Hence, increasing oxygen vacancy concentration usually enhances catalytic performance, consistent with the XPS analysis results.

H_2-TPR measurement was implemented to assess the reducibility of synthesized MnO_x catalysts, with relevant profiles presented in Figure 5b. Clearly, the curves of catalysts presented two obvious reduction peaks, while the peak at 300~400 °C belonged to Mn^{4+} to Mn^{3+} transformation ($MnO_2 \rightarrow Mn_2O_3$) and another one (400~500 °C) was assigned to Mn^{3+} to Mn^{2+} reduction ($Mn_2O_3 \rightarrow MnO$), respectively, corresponding to the main existence of Mn^{4+} and Mn^{3+} from XPS analysis [39,40]. For the peaks at lower temperature (300~400 °C), the temperature of reduction peaks ranked as MnO_x-II < MnO_x-III < MnO_x-I < MnO_x-IV. Lower reduction temperature usually means better reducibility, which can promote oxygen species migration and mobility [41,42]. The reduction temperature of MnO_x-IV was relatively higher, corresponding to its weak reducibility and poor catalytic activity. With better redox ability at lower temperatures, the low-temperature activity of MnO_x-II would be greatly promoted.

To analyze the acidity of MnO_x catalysts, the NH_3-TPD profiles are presented in Figure 5c. With desorption temperature increasing, the two peaks were ascribed to Lewis acid sites (physisorbed NH_3 and NH_4^+) and Brönsted acid sites (desorption of NH_4^+), respectively [43]. Generally, surface acidity is of great importance in the removal procedure of VOCs, covering reactant adsorption, ozone decomposition, and resultant desorption [44]. Notably, Lewis acid sites are closely correlated to reactive oxygen species formation and C–C bond breaking, which facilitate the further reaction of HCHO [45,46]. With desirable catalytic activity, MnO_x-II showed a lower desorption temperature (86 °C) and more Lewis acid sites, signifying its better acidity at lower temperatures, which would facilitate the degradation of HCHO indoors.

2.3. Effect of H_2O

As an inevitable component in indoor air, water vapor (H_2O) is known to be a possible influence factor for catalytic performance. In the long-time H_2O resistance test, two different concentrations of H_2O (RH = 50% and RH = 100%) were added to reaction gas (Figure 6). Meanwhile, the HCHO conversion and outlet CO_2 selectivity over MnO_x-II catalyst at 30 °C were monitored during the test, with an O_3/HCHO ratio of 2.0. With the addition of a low concentration of H_2O (RH = 50%), the HCHO conversion was basically unchanged after 2 h. Subsequently, introducing a higher concentration of H_2O (RH = 100%), the HCHO conversion slightly decreased to a stable platform at ~97% and then gradually recovered to ~99% after stopping H_2O. Evidently, H_2O of high concentration resulted in catalyst poisoning to a certain extent, and the slight deactivation was fortunately reversible. In addition, the outlet CO_2 selectivity obviously increased when introducing H_2O, as the generated OH active radicals may be conducive to the complete oxidation of HCHO [47]. Moreover, the stability test was conducted, and the HCHO conversion was maintained at ~100% for 7 h, demonstrating the desirable stability of MnO_x-II.

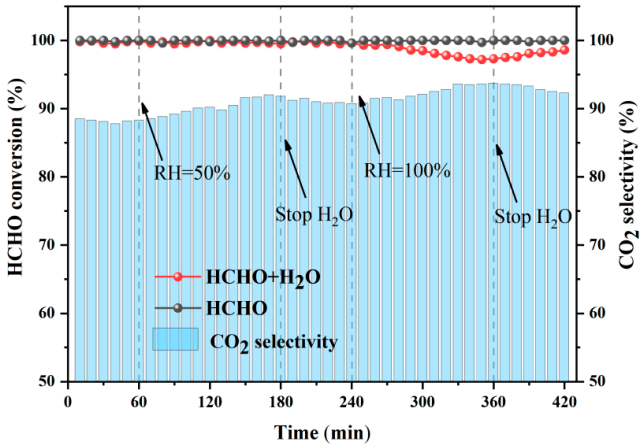

Figure 6. Effect of H_2O on HCHO catalytic ozoantion over MnO_x-II catalyst.

2.4. In-Situ DRIFTS Measurement

To study the HCHO ozonation reaction mechanism on MnO_x-II catalysts, in situ DRIFTS spectra were collected to record the evolution of intermediate products. As shown in Figure 7a, the dynamic changes in the HCHO adsorption process (30 ppm HCHO+N_2) at ambient temperature were conducted with the change in reaction time. Typically, the peaks located between 800 and 1200 cm^{-1} were identified as DOM species [48]. While the bands at 1579 cm^{-1} and 1376 cm^{-1} were ascribed to the asymmetric and symmetric (COO) stretch vibration of formates, respectively. Also, the band at 2858 cm^{-1} was associated with various hydrocarbon vibrations [49]. Additionally, the peaks at 3690 and 1350 cm^{-1} belonged to hydroxyl groups and carbonate species, respectively [50]. The weak inverse peaks of hydroxyl groups may reflect the utilization of OH groups and the continuous regeneration, possibly facilitating the further conversion of DOM species [51].

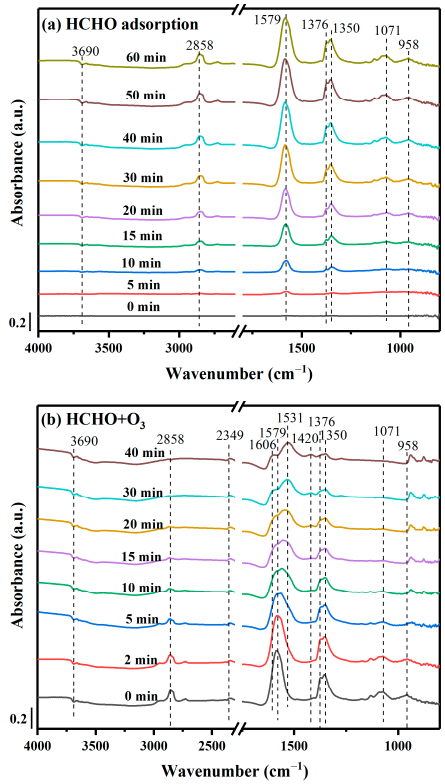

Figure 7. In-situ DRIFTS analysis of HCHO degradation mechanism on MnO_x-II catalyst (Reaction conditions: (**a**) 30 ppm HCHO; (**b**) addition of 90 ppm O_3).

When the adsorption of HCHO was saturated, 90 ppm O_3 was added to the feed gas. Clearly, the intensity of DOM bands (1071 and 958 cm^{-1}) gradually disappeared, as presented in Figure 7b. Simultaneously, the peaks of formate species (1376, 1579, and 2858 cm^{-1}) decreased with time, and the peaks corresponding to different modes of carbonate species, such as hydrocarbonate species (1606 cm^{-1}), bicarbonate species (1420 cm^{-1}) and monodentate carbonate species (1531 cm^{-1}) emerged [52]. Moreover, the band that appeared at 2349 cm^{-1} corresponded to CO_2 formation as the ideal final product. And the band of hydroxyl groups (3690 cm^{-1}) was basically unchanged, which may be replenished by the generated H_2O during the HCHO catalytic ozonation.

2.5. Theoretical Calculation and Reaction Mechanism

For heterogeneous catalysis, the adsorption of reactants on MnO_x catalysts with α-Mn_2O_3 structure was an important process [53]. To find out the role of oxygen vacancies in the reactant adsorption procedure, the adsorption energies and bond lengths of O_3 and HCHO on the α-Mn_2O_3 (1 1 1) surface were evaluated (Figure 8). With an oxygen vacancy (V_0), the calculated O_3 adsorption energy (−0.46 eV) and Mn-O distance (1.935 Å) were lower than the original ones (E_{ads} = −0.34 eV, L_{Mn-O} = 1.951 Å). As for the adsorption of HCHO, the adsorption energy was −0.36 eV, higher than the configuration with V_0 (E_{ads} = −0.52 eV), and the Mn–O bond length was in the same situation (L_{Mn-O} = 2.44 Å, L_{Mn-O} = 2.34 Å with V_0). Typically, more negative adsorption energies and shorter bond lengths always indicate an enhanced interaction between reactants and catalytic surfaces [54]. Thus, the existence of oxygen vacancies may promote reactant adsorption and consequently accelerate catalytic reaction.

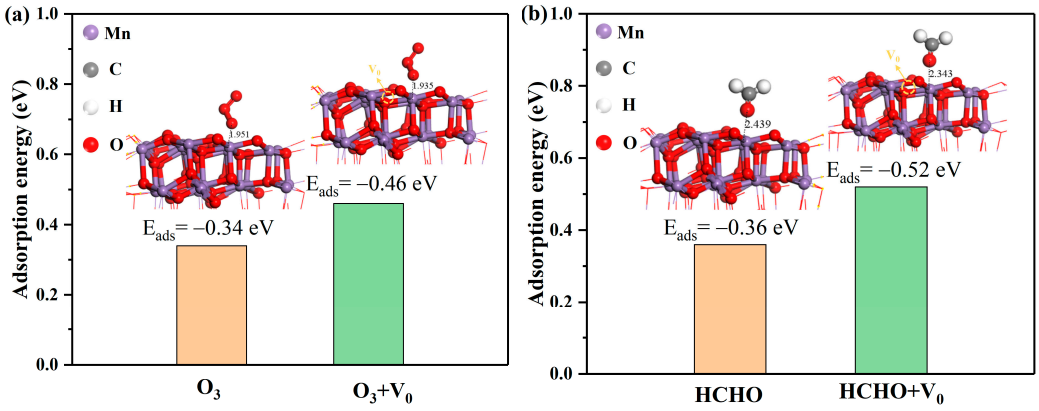

Figure 8. The E_{ads} and bond length of (**a**) O_3 and (**b**) HCHO on the α-Mn_2O_3 (1 1 1) surface (V_0 referred to oxygen vacancy).

In summary, coupling in situ DRIFTS with DFT analysis, a feasible reaction route of HCHO catalytic ozonation is depicted in Figure 9. Firstly, with the promotion of oxygen vacancies, the adsorption process of HCHO and O_3 on surface reactive sites of MnO_x catalysts occurred. And then the active oxygen species immediately converted HCHO into DOM species, while the surface reactive hydroxyl groups were related to the formation of formate species. Then, on the surface oxygen vacancies, O_3 was quickly decomposed to O_2 molecules and reactive oxygen radicals (O*). Finally, formate species were further oxidized into carbonic acid and decomposed to form CO_2 and H_2O, producing harmless degradation products.

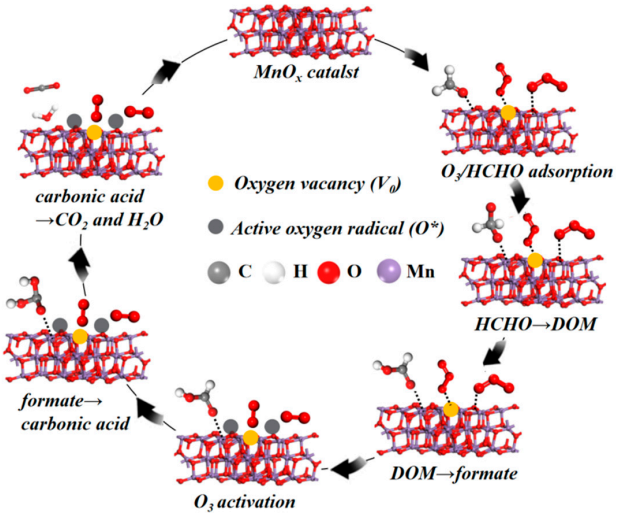

Figure 9. Possible route for HCHO catalytic ozonation on MnO_x catalysts.

3. Materials and Methods

3.1. Catalyst Preparation

For the synthesis of MnO_x-I, 5 mmol $Mn(CH_3COO)_2{\cdot}4H_2O$ (Aladdin, Shanghai, China) and 15 mmol H_3BTC (Aladdin, China) were placed in deionized (DI) water and ethanol (Sinopharm, China), respectively. Next, they would be vigorously blended and kept under constant stirring (25 °C, 15 h).

To obtain MnO_x-II, 5 mmol $Mn(CH_3COO)_2{\cdot}4H_2O$ and a certain amount of PVP (Aladdin, China) were dispersed in a mixture solution (vol ratio of C_2H_5OH and H_2O was 2:1) (A solution). Next, 10 mmol H_3BTC was dissolved in the same C_2H_5OH/H_2O (2:1) solution (B solution). Subsequently, after the thorough mixing of A and B, the admixture was left to stand for 12 h at ambient temperature.

During the typical synthesis of MnO_x-III, 0.1 mol/L $Mn(CH_3COO)_2{\cdot}4H_2O$ (5 mmol) solution and 0.1 mol/L 8-hydroxyquinoline (10 mmol) (Aladdin, Shanghai, China) solution were mixed vigorously and maintained for 5 h at normal temperature.

Typically, the MnO_x-IV was synthesized by the co-precipitation method for comparison via the intensive mixing of $Mn(CH_3COO)_2{\cdot}4H_2O$ solution and NaOH (Sinopharm, Beijing, China) solution.

All the samples were separated through centrifugation and washed with DI water and ethanol. After being totally dried and then annealed at 500 °C for 3 h, the obtained catalysts were ground to 40~60 mesh. In summary, the synthesis scheme of MOF-derived MnO_x catalysts is presented in Figure 10.

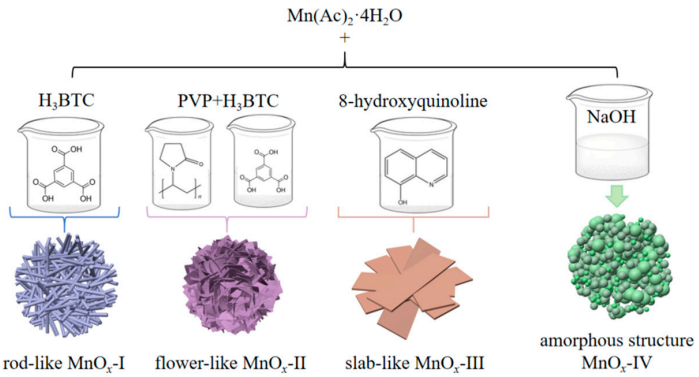

Figure 10. The preparation scheme of MOFs-derived MnO_x catalysts.

3.2. Catalytic Activity

The catalytic ozonation of HCHO over synthesized catalysts was performed on an experimental setup, as depicted in Figure S2. Meanwhile, the detailed procedures were summarized in Supporting Information (Text S1).

The catalytic activity was evaluated by conversion efficiencies of HCHO and O_3, and the selectivity of CO and CO_2, which were calculated with the following equations:

$$[\mathrm{HCHO}]\mathrm{conv.} = \frac{[\mathrm{CO}]\mathrm{outlet} + [\mathrm{CO_2}]\mathrm{outlet}}{[\mathrm{HCHO}]\mathrm{initial}} \times 100\% \quad (3)$$

$$[\mathrm{O_3}]\mathrm{conv.} = \frac{[\mathrm{O_3}]\mathrm{initial} - [\mathrm{O_3}]\mathrm{outlet}}{[\mathrm{O_3}]\mathrm{initial}} \times 100\% \quad (4)$$

$$[\mathrm{CO_2}]\mathrm{selec.} = \frac{[\mathrm{CO_2}]\mathrm{outlet}}{[\mathrm{CO}]\mathrm{outlet} + [\mathrm{CO_2}]\mathrm{outlet}} \times 100\% \quad (5)$$

where $[HCHO]_{initial}$ and $[O_3]_{initial}$ are the initial concentration of HCHO and O_3, unit ppm, respectively. $[CO]_{outlet}$, $[CO_2]_{outlet}$ and $[O_3]_{outlet}$ are the outlet concentration of CO, CO_2 and O_3, unit ppm, respectively.

3.3. Catalyst Characterization

The samples were evaluated by XRD, SEM, XPS, BET, NH_3-TPD, H_2-TPR, and in situ DRIFTS characterizations. And the materials in detail are presented in Supporting Information (Text S2).

3.4. DFT Calculation

The DFT calculations were conducted with the CASTEP package using Material Studio software 2019 [55]. And the exchange–correlation interaction was processed with the generalized gradient approximation (GGA) using the Perdew–Burke–Enzerhof (PBE) function. A 650 eV cutoff energy was adopted for all DFT calculations. From XRD analysis, a an α-Mn_2O_3 phase of MnO_x catalysts was confirmed, and the Mn_2O_3 (1 1 1) surface was cleaved, as shown in Figure S3 [56,57]. And a 16 Å vacuum layer was introduced in the z-direction to eliminate the next layer's influence. The adsorption energy (Eads) of adsorbates on the catalyst surface was determined by the equation below:

$$E_{ads} = E_{(adsorbate\text{-}catalyst)} - (E_{catalyst} + E_{adsorbate}) \quad (6)$$

where $E_{(adsorbate\text{-}catalyst)}$ is the total energy of catalyst-adsorbate system, $E_{catalyst}$ is the total energy of catalyst, and $E_{adsorbate}$ is the total energy of the gas-phase molecule.

4. Conclusions

To completely remove HCHO under room temperature, the catalytic ozonation method with higher efficiency and fewer byproducts is an efficient way. Herein, a series of efficient MOF-derived MnO_x catalysts with distinct shapes were fabricated via a facile sacrificial template strategy for HCHO catalytic ozonation. The flower-like MnO_x-II catalyst showed excellent catalytic activity (100% HCHO conversion, O_3/HCHO = 1.5) and higher CO_2 selectivity (above 90%, O_3/HCHO = 2.5), while the MnO_x-IV prepared by the co-precipitation method exhibited poor catalytic performance. The unique flower-like structure of MnO_x-II endows it with expanded surface area and abundant surface active sites, facilitating the catalytic ozonation process of HCHO. Moreover, its higher Mn^{3+} and O_{ad} content promoted the formation of oxygen vacancies, as verified by Raman spectra. Therefore, the presence of oxygen vacancies appears crucial for catalysis, accelerating reactant adsorption, ozone decomposition, and complete oxidation of HCHO. In addition, the better acidity and re-

ducibility, sufficient active oxygen species, and improved oxygen mobility also contributed to the excellent activity of MnO_x-II. In stability and H_2O tolerance experiments, MnO_x-II maintained ~100% HCHO conversion without H_2O and ~97% HCHO conversion when RH = 100%, respectively. Based on DFT calculation, the crucial role of oxygen vacancies in promoting HCHO and O_3 adsorption process was elucidated. Moreover, through the detection of intermediate products, a feasible catalytic mechanism was raised (HCHO, DOM, formates, H_2CO_3, H_2O+CO_2, successively).

Supplementary Materials: The following supporting information can be downloaded at: https://www.mdpi.com/article/10.3390/catal15080752/s1, Figure S1: N_2 adsorption-desorption isotherms and distribution curves of pore size of synthesized catalysts.; Figure S2: Schematic of experimental set-up; Figure S3: Schematic structure model of Mn_2O_3 (1 1 1) surface.

Author Contributions: Y.S.: investigation, conceptualization, methodology, validation, writing original draft. Y.Z. (Yiwei Zhang): writing—review and editing, conceptualization. Y.H.: project administration, resources, methodology. W.W.: conceptualization, supervision, project administration. Y.Z. (Yanqun Zhu): writing—review and editing. Z.W.: writing—review and editing, methodology, supervision, funding acquisition. All authors have read and agreed to the published version of the manuscript.

Funding: This research was supported by the "Pioneer" and "Leading Goose" R&D Program of Zhejiang (2023C03126), the National Natural Science Foundation of China (52125605), and the Fundamental Research Funds for the Central Universities (2022ZFJH04).

Data Availability Statement: Data will be made available on request.

Conflicts of Interest: The authors declare no conflicts of interest.

References

1. Hequet, V.; Raillard, C.; Debono, O.; Thévenet, F.; Locoge, N.; Le Coq, L. Photocatalytic oxidation of VOCs at ppb level using a closed-loop reactor: The mixture effect. *Appl. Catal. B Environ.* **2018**, *226*, 473–486. [CrossRef]
2. Ji, J.; Lu, X.; Chen, C.; He, M.; Huang, H. Potassium-modulated δ-MnO_2 as robust catalysts for formaldehyde oxidation at room temperature. *Appl. Catal. B Environ.* **2020**, *260*, 118210. [CrossRef]
3. He, C.; Wang, Y.; Li, Z.; Huang, Y.; Liao, Y.; Xia, D.; Lee, S. Facet engineered α-MnO_2 for efficient catalytic ozonation of odor CH_3SH: Oxygen vacancy-induced active centers and catalytic mechanism. *Environ. Sci. Technol.* **2020**, *54*, 12771–12783. [CrossRef]
4. Zhang, C.; He, H.; Tanaka, K.I. Perfect catalytic oxidation of formaldehyde over a Pt/TiO_2 catalyst at room temperature. *Catal. Commun.* **2005**, *6*, 211–214. [CrossRef]
5. Qu, J.; Chen, D.; Li, N.; Xu, Q.; Li, H.; He, J.; Lu, J. 3D gold-modified cerium and cobalt oxide catalyst on a graphene aerogel for highly efficient catalytic formaldehyde oxidation. *Small* **2019**, *15*, 1804415. [CrossRef] [PubMed]
6. Chen, Y.; Lv, D.; Wu, J.; Xiao, J.; Xi, H.; Xia, Q.; Li, Z. A new MOF-505@GO composite with high selectivity for CO_2/CH_4 and CO_2/N_2 separation. *Chem. Eng. J.* **2017**, *308*, 1065–1072. [CrossRef]
7. Chen, M.; Yin, H.; Li, X.; Qiu, Y.; Cao, G.; Wang, J.; Yang, X.; Wang, P. Facet-and defect-engineered Pt/Fe_2O_3 nanocomposite catalyst for catalytic oxidation of airborne formaldehyde under ambient conditions. *J. Hazard. Mater.* **2020**, *395*, 122628. [CrossRef]
8. Guan, S.; Li, W.; Ma, J.; Lei, Y.; Zhu, Y.; Huang, Q.; Dou, X. A review of the preparation and applications of MnO2 composites in formaldehyde oxidation. *J. Ind. Eng. Chem.* **2018**, *66*, 126–140. [CrossRef]
9. Zhu, D.; Huang, Y.; Li, R.; Huang, T.; Cao, J.J.; Shen, Z.; Lee, S.C. Formaldehyde oxidation over Co@N-doped carbon at room temperature: Tunable Co size and intensified surface electron density. *ACS EST Eng.* **2021**, *1*, 917–927. [CrossRef]
10. Guo, Y.; Wen, M.; Li, G.; An, T. Recent advances in VOC elimination by catalytic oxidation technology onto various nanoparticles catalysts: A critical review. *Appl. Catal. B Environ.* **2021**, *281*, 119447. [CrossRef]
11. Zhu, G.; Zhu, J.; Jiang, W.; Zhang, Z.; Wang, J.; Zhu, Y.; Zhang, Q. Surface oxygen vacancy induced α-MnO_2 nanofiber for highly efficient ozone elimination. *Appl. Catal. B Environ.* **2017**, *209*, 729–737. [CrossRef]
12. Wang, F.; Dai, H.; Deng, J.; Bai, G.; Ji, K.; Liu, Y. Manganese oxides with rod-, wire-, tube-, and flower-like morphologies: Highly effective catalysts for the removal of toluene. *Environ. Sci. Technol.* **2012**, *46*, 4034–4041. [CrossRef] [PubMed]
13. Xiang, L.; Lin, F.; Cai, B.; Li, G.; Zhang, L.; Wang, Z.; Yan, B.; Wang, Y.; Chen, G. Catalytic ozonation of CH_2Cl_2 over hollow urchin-like MnO_2 with regulation of active oxygen by catalyst modification and ozone promotion. *J. Hazard. Mater.* **2022**, *436*, 129217. [CrossRef] [PubMed]

14. Dezhi, Z.; Tianying, D.; Xiaosong, L.I.; Jinglin, L.I.U.; Chuan, S.H.I.; Aimin, Z.H.U. Ozone catalytic oxidation of HCHO in air over MnOx at room temperature. *Chin. J. Catal.* **2012**, *33*, 396–401. [CrossRef]
15. Tadéa, M.O.; Wanga, S. Shape-controlled activation of peroxymonosulfate by single crystal-Mn_2O_3 for catalytic phenol degradation in aqueous solution. *Appl. Catal. B Environ.* **2014**, *154*, 246–251.
16. Zhao, Q.; Du, Q.; Yang, Y.; Zhao, Z.; Cheng, J.; Bi, F.; Shi, X.; Xu, J.; Zhang, X. Effects of regulator ratio and guest molecule diffusion on VOCs adsorption by defective UiO-67: Experimental and theoretical insights. *Chem. Eng. J.* **2022**, *433*, 134510. [CrossRef]
17. Huang, C.; Ji, Q.; Zhang, H.; Wang, Y.; Wang, S.; Liu, X.; Guo, Y.; Zhang, C. Ru-incorporated Co_3O_4 nanoparticles from self-sacrificial ZIF-67 template as efficient bifunctional electrocatalysts for rechargeable metal-air battery. *J. Colloid Interface Sci.* **2022**, *606*, 654–665. [CrossRef]
18. Chen, J.; Yang, Y.; Zhao, S.; Bi, F.; Song, L.; Liu, N.; Xu, J.; Wang, Y.; Zhang, X. Stable black phosphorus encapsulation in porous mesh-like UiO-66 promoted charge transfer for photocatalytic oxidation of toluene and o-dichlorobenzene: Performance, degradation pathway, and mechanism. *ACS Catal.* **2022**, *12*, 8069–8081. [CrossRef]
19. Bi, F.; Zhao, Z.; Yang, Y.; Liu, Q.; Huang, W.; Huang, Y.; Zhang, X. Efficient degradation of toluene over ultra-low Pd supported on UiO-66 and its functional materials: Reaction mechanism, water-resistance, and influence of SO_2. *Environ. Funct. Mater.* **2022**, *1*, 166–181. [CrossRef]
20. Yuan, K.; Song, T.; Wang, D.; Zhang, X.; Gao, X.; Zou, Y.; Dong, H.; Tang, Z.; Hu, W. Effective and Selective Catalysts for Cinnamaldehyde Hydrogenation: Hydrophobic Hybrids of Metal–Organic Frameworks, Metal Nanoparticles, and Micro-and Mesoporous Polymers. *Angew. Chem. Int. Ed.* **2018**, *57*, 5708–5713. [CrossRef]
21. Kumar, P.; Kim, K.H.; Kwon, E.E.; Szulejko, J.E. Metal–organic frameworks for the control and management of air quality: Advances and future direction. *J. Mater. Chem. A* **2016**, *4*, 345–361. [CrossRef]
22. Salunkhe, R.R.; Kaneti, Y.V.; Yamauchi, Y. Metal–organic framework-derived nanoporous metal oxides toward supercapacitor applications: Progress and prospects. *ACS Nano* **2017**, *11*, 5293–5308. [CrossRef] [PubMed]
23. Zhang, X.; Lv, X.; Bi, F.; Lu, G.; Wang, Y. Highly efficient Mn_2O_3 catalysts derived from Mn-MOFs for toluene oxidation: The influence of MOFs precursors. *Mol. Catal.* **2020**, *482*, 110701. [CrossRef]
24. Li, J.; Mo, S.; Ding, X.; Huang, L.; Zhou, X.; Fan, Y.; Zhang, Y.; Fu, M.; Xie, Q.; Ye, D. Hollow cavity engineering of MOFs-derived hierarchical MnOx structure for highly efficient photothermal degradation of ethyl acetate under light irradiation. *Chem. Eng. J.* **2023**, *464*, 142412. [CrossRef]
25. Cheng, L.; Men, Y.; Wang, J.; Wang, H.; An, W.; Wang, Y.; Duan, Z.; Liu, J. Crystal facet-dependent reactivity of α-Mn_2O_3 microcrystalline catalyst for soot combustion. *Appl. Catal. B Environ.* **2017**, *204*, 374–384. [CrossRef]
26. Mei, J.; Shen, Y.; Wang, Q.; Shen, Y.; Li, W.; Zhao, J.; Chen, J.; Zhang, S. Roles of oxygen species in low-temperature catalytic o-xylene oxidation on MOF-derived bouquetlike CeO_2. *ACS Appl. Mater. Interfaces* **2022**, *14*, 35694–35703. [CrossRef]
27. Wang, Y.; Wang, G.; Deng, W.; Han, J.; Qin, L.; Zhao, B.; Guo, L.; Xing, F. Study on the structure-activity relationship of Fe-Mn oxide catalysts for chlorobenzene catalytic combustion. *Chem. Eng. J.* **2020**, *395*, 125172. [CrossRef]
28. Zheng, Y.; Zhao, Q.; Shan, C.; Lu, S.; Su, Y.; Han, R.; Song, C.; Ji, N.; Ma, D.; Liu, Q. Enhanced acetone oxidation over the CeO_2/Co_3O_4 catalyst derived from metal– organic frameworks. *ACS Appl. Mater. Interfaces* **2020**, *12*, 28139–28147. [CrossRef]
29. Yang, P.; Yang, S.; Shi, Z.; Meng, Z.; Zhou, R. Deep oxidation of chlorinated VOCs over CeO_2-based transition metal mixed oxide catalysts. *Appl. Catal. B Environ.* **2015**, *162*, 227–235. [CrossRef]
30. Zhou, T.; Cao, S.; Zhang, R.; Tu, J.; Fei, T.; Zhang, T. Effect of cation substitution on the gas-sensing performances of ternary spinel MCo_2O_4 (M = Mn, Ni, and Zn) multishelled hollow twin spheres. *ACS Appl. Mater. Interfaces* **2019**, *11*, 28023–28032. [CrossRef]
31. Pei, W.; Liu, Y.; Deng, J.; Zhang, K.; Hou, Z.; Zhao, X.; Dai, H. Partially embedding Pt nanoparticles in the skeleton of 3DOM Mn_2O_3: An effective strategy for enhancing catalytic stability in toluene combustion. *Appl. Catal. B Environ.* **2019**, *256*, 117814. [CrossRef]
32. Jia, J.; Zhang, P.; Chen, L. Catalytic decomposition of gaseous ozone over manganese dioxides with different crystal structures. *Appl. Catal. B Environ.* **2016**, *189*, 210–218. [CrossRef]
33. Gopi, T.; Swetha, G.; Shekar, S.C.; Ramakrishna, C.; Saini, B.; Krishna, R.; Rao, P.V.L. Catalytic decomposition of ozone on nanostructured potassium and proton containing δ-MnO_2 catalysts. *Catal. Commun.* **2017**, *92*, 51–55. [CrossRef]
34. Li, J.R.; Zhang, W.P.; Li, C.; He, C. Efficient catalytic degradation of toluene at a readily prepared Mn-Cu catalyst: Catalytic performance and reaction pathway. *J. Colloid Interface Sci.* **2021**, *591*, 396–408. [CrossRef]
35. Nawaz, F.; Cao, H.; Xie, Y.; Xiao, J.; Chen, Y.; Ghazi, Z.A. Selection of active phase of MnO_2 for catalytic ozonation of 4-nitrophenol. *Chemosphere* **2017**, *168*, 1457–1466. [CrossRef] [PubMed]
36. Piumetti, M.; Fino, D.; Russo, N. Mesoporous manganese oxides prepared by solution combustion synthesis as catalysts for the total oxidation of VOCs. *Appl. Catal. B Environ.* **2015**, *163*, 277–287. [CrossRef]
37. Wang, P.; Wang, J.; An, X.; Shi, J.; Shangguan, W.; Hao, X.; Xu, G.; Tang, B.; Abudula, A.; Guan, G. Generation of abundant defects in Mn-Co mixed oxides by a facile agar-gel method for highly efficient catalysis of total toluene oxidation. *Appl. Catal. B Environ.* **2021**, *282*, 119560. [CrossRef]

38. Sun, Y.; Zhang, X.; Li, N.; Xing, X.; Yang, H.; Zhang, F.; Cheng, J.; Zhang, Z.; Hao, Z. Surface properties enhanced MnxAlO oxide catalysts derived from MnxAl layered double hydroxides for acetone catalytic oxidation at low temperature. *Appl. Catal. B Environ.* **2019**, *251*, 295–304. [CrossRef]
39. Liu, X.; Liu, J.; Chen, J.; Zhong, F. Mn_2O_3/γ-Al_2O_3 catalysts synergistic double dielectric barrier discharge (DDBD) degradation of toluene, ethyl-acetate and acetone. *Chemosphere* **2021**, *284*, 131299. [CrossRef]
40. Zhao, L.; Zhang, Z.; Li, Y.; Leng, X.; Zhang, T.; Yuan, F.; Niu, X.; Zhu, Y. Synthesis of Ce-MnOx hollow microsphere with hierarchical structure and its excellent catalytic performance for toluene combustion. *Appl. Catal. B Environ.* **2019**, *245*, 502–512. [CrossRef]
41. Wang, D.T.; Guo, N.; Jiang, L.X.; Lian, S.Z.; Wang, Z.W. Metal organic frameworks derived metal oxides prepared by oxygen vacancy engineering with the enhanced catalytic activity for toluene oxidation. *J. Environ. Chem. Eng.* **2022**, *10*, 108798. [CrossRef]
42. Wang, Y.; Deng, W.; Wang, Y.; Guo, L.; Ishihara, T. A comparative study of the catalytic oxidation of chlorobenzene and toluene over Ce-Mn oxides. *Mol. Catal.* **2018**, *459*, 61–70. [CrossRef]
43. Shao, J.; Lin, F.; Wang, Z.; Liu, P.; Tang, H.; He, Y.; Cen, K. Low temperature catalytic ozonation of toluene in flue gas over Mn-based catalysts: Effect of support property and SO_2/water vapor addition. *Appl. Catal. B Environ.* **2020**, *266*, 118662. [CrossRef]
44. Sun, P.; Wang, W.; Dai, X.; Weng, X.; Wu, Z. Mechanism study on catalytic oxidation of chlorobenzene over MnxCe1-xO2/H-ZSM5 catalysts under dry and humid conditions. *Appl. Catal. B Environ.* **2016**, *198*, 389–397. [CrossRef]
45. Weng, X.; Sun, P.; Long, Y.; Meng, Q.; Wu, Z. Catalytic oxidation of chlorobenzene over MnxCe1-xO2/HZSM-5 catalysts: A study with practical implications. *Environ. Sci. Technol.* **2017**, *51*, 8057–8066. [CrossRef]
46. Tian, M.; Guo, X.; Dong, R.; Guo, Z.; Shi, J.; Yu, Y.; Cheng, M.; Albilali, R.; He, C. Insight into the boosted catalytic performance and chlorine resistance of nanosphere-like meso-macroporous CrOx/MnCo3Ox for 1, 2-dichloroethane destruction. *Appl. Catal. B Environ.* **2019**, *259*, 118018. [CrossRef]
47. Tang, H.; Wang, Z.; Shao, J.; Lin, F.; Liu, P.; He, Y.; Zhu, Y. Catalytic decomposition of residual ozone over cactus-like MnO2 nanosphere: Synergistic mechanism and SO_2/H_2O interference. *ACS Omega* **2022**, *7*, 9818–9833. [CrossRef]
48. Li, C.; Domen, K.; Maruya, K.I.; Onishi, T. Spectroscopic identification of adsorbed species derived from adsorption and decomposition of formic acid, methanol, and formaldehyde on cerium oxide. *J. Catal.* **1990**, *125*, 445–455. [CrossRef]
49. Zhu, L.; Wang, J.; Rong, S.; Wang, H.; Zhang, P. Cerium modified birnessite-type MnO_2 for gaseous formaldehyde oxidation at low temperature. *Appl. Catal. B Environ.* **2017**, *211*, 212–221. [CrossRef]
50. Zhang, C.; Liu, F.; Zhai, Y.; Ariga, H.; Yi, N.; Liu, Y.; Asakura, K.; Flytzani-Stephanopoulos, M.; He, H. Alkali-metal-promoted Pt/TiO_2 opens a more efficient pathway to formaldehyde oxidation at ambient temperatures. *Angew. Chem. Int. Ed.* **2012**, *51*, 9628–9632. [CrossRef]
51. Yan, Z.; Xu, Z.; Cheng, B.; Jiang, C. Co_3O_4 nanorod-supported Pt with enhanced performance for catalytic HCHO oxidation at room temperature. *Appl. Surf. Sci.* **2017**, *404*, 426–434. [CrossRef]
52. Wang, H.; Guo, W.; Jiang, Z.; Yang, R.; Jiang, Z.; Pan, Y.; Shangguan, W. New insight into the enhanced activity of ordered mesoporous nickel oxide in formaldehyde catalytic oxidation reactions. *J. Catal.* **2018**, *361*, 370–383. [CrossRef]
53. Collins, S.S.; Cittadini, M.; Pecharromán, C.; Martucci, A.; Mulvaney, P. Hydrogen spillover between single gold nanorods and metal oxide supports: A surface plasmon spectroscopy study. *Acs Nano* **2015**, *9*, 7846–7856. [CrossRef]
54. Zhao, L.; Yang, Y.; Liu, J.; Ding, J. Mechanistic insights into benzene oxidation over $CuMn_2O_4$ catalyst. *J. Hazard. Mater.* **2022**, *431*, 128640. [CrossRef]
55. Segall, M.D.; Lindan, P.J.; Probert, M.A.; Pickard, C.J.; Hasnip, P.J.; Clark, S.J.; Payne, M.C. First-principles simulation: Ideas, illustrations and the CASTEP code. *J. Phys. Condens. Matter* **2002**, *14*, 2717. [CrossRef]
56. Xin, Y.; Cheng, L.; Lv, Y.; Jia, J.; Han, D.; Zhang, N.; Wang, J.; Zhang, Z.; Cao, X.M. Experimental and theoretical insight into the facet-dependent mechanisms of NO oxidation catalyzed by structurally diverse Mn_2O_3 nanocrystals. *ACS Catal.* **2021**, *12*, 397–410. [CrossRef]
57. Yan, H.; Shen, Q.; Sun, Y.; Zhao, S.; Lu, R.; Gong, M.; Liu, Y.; Zhou, X.; Jin, X.; Yang, C.; et al. Tailoring facets of α-Mn_2O_3 microcrystalline catalysts for enhanced selective oxidation of glycerol to glycolic acid. *ACS Catal.* **2021**, *11*, 6371–6383. [CrossRef]